

## STEM CELLS AND REGENERATION

### **RESEARCH ARTICLE**

# Control of gastruloid patterning and morphogenesis by the Erk and Akt signaling pathways

Evan J. Underhill<sup>1</sup> and Jared E. Toettcher<sup>2,\*</sup>

#### **ABSTRACT**

Many developmental processes rely on the localized activation of receptor tyrosine kinases and their canonical downstream effectors Erk and Akt, yet the specific roles played by each of these signals is still poorly understood. Gastruloids, 3D cell culture models of mammalian gastrulation and axial elongation, enable quantitative dissection of signaling patterns and cell responses in a simplified, experimentally accessible context. We find that mouse gastruloids contain posterior-to-anterior gradients of Erk and Akt phosphorylation induced by distinct receptor tyrosine kinases, with features of the Erk pattern and expression of its downstream target Snail exhibiting hallmarks of size-invariant scaling. Both Erk and Akt signaling contribute to cell proliferation, whereas Erk activation is also sufficient to induce Snail expression and precipitate profound tissue shape changes. We further uncover that Erk signaling is sufficient to convert the entire gastruloid to one of two mesodermal fates depending on position along the anteroposterior axis. In all, these data demonstrate functional roles for two core signaling gradients in mammalian development and suggest how these modules might be harnessed to engineer user-defined tissues with predictable shapes and cell fates.

KEY WORDS: Gastruloid, Morphogenesis, Cell signaling

## **INTRODUCTION**

Embryos undergo both dramatic physical transformations and complex sequences of cell differentiation on their path from single cell to mature organism. In many cases, these developmental transitions are controlled by localized patterns of receptor tyrosine kinase (RTK) activity that arise either as a consequence of other localized cues (e.g. terminal pattern in the early *Drosophila* embryo; Li, 2005) or spontaneously through self-organization [e.g. fibroblast growth factor (FGF)-dependent cell fate choices in the mammalian blastocyst; Chazaud et al., 2006]. One particularly well-studied example of RTK-driven morphogenesis and differentiation occurs during vertebrate anterior-posterior (A-P) axis elongation, during which the posterior domain of the embryo unidirectionally elongates as proliferative neuromesodermal progenitors (NMPs) differentiate into either neural ectoderm or mesoderm (Tzouanacou et al., 2009). FGF, an RTK ligand that is present in a posteriorto-anterior gradient in the embryonic day (E) 9.0 mouse embryo (Dubrulle and Pourquié, 2004), is necessary for proper elongation

<sup>1</sup>Department of Chemical & Biological Engineering, Princeton University, Princeton, NJ 08544, USA. <sup>2</sup>Department of Molecular Biology, Princeton University, Princeton,

\*Author for correspondence (toettcher@princeton.edu)

D J.E.T., 0000-0002-1546-4030

Handling Editor: Matthias Lutolf Received 31 January 2023; Accepted 11 July 2023

and differentiation:  $Fgfr1^{-/-}$  mutant embryos and Fgf4/8 conditional knockout mice exhibit growth defects and contain ectopic neural tubes at the expense of mesoderm formation (Boulet and Capecchi, 2012; Ciruna and Rossant, 2001; Ciruna et al., 1997; Yamaguchi et al., 1994).

FGF receptors (FGFRs) have been widely observed to regulate a broad range of canonical effector pathways (Brewer et al., 2016). Two such pathways, the Ras/Erk and PI3K/Akt signaling cascades, also exhibit graded activity along the A-P axis of the lategastrulation mouse embryo (Dubrulle and Pourquié, 2004; Niwa et al., 2011). Yet, despite extensive genetic study, many questions remain about the contributions of these two pathways during posterior elongation. Do Erk (Mapk1/Mapk3) and Akt (Akt1/Akt2/ Akt3) play distinct or overlapping roles in driving cellular responses? Are both pathways indeed dependent on graded FGFR activity or do they respond to more complex combinations of upstream stimuli? Finally, although loss-of-function genetic mutants have defined necessary signals for A-P axial elongation and patterned gene expression, much less is known about the consequences of ectopic pathway activation. Which signals are sufficient to drive changes in morphogenesis and germ layer specification?

Embryonic organoids can provide a window into early development in a reduced-complexity context, while also circumventing the experimental challenges of the post-implantation mammalian embryo. The mouse gastruloid, for example, is a model system that can recapitulate many developmental processes, including the formation of the three body axes, A-P axial elongation, Hox gene patterning, and even somitogenesis (Beccari et al., 2018; van den Brink et al., 2020; Veenvliet et al., 2020). Beginning from a collection of mouse embryonic stem cells (mESCs), gastruloids spontaneously develop asymmetric gene expression over the course of 4 days, followed by the emergence and rapid outgrowth of a tissue domain in a process resembling posterior elongation in the embryo. This quick and reproducible development, coupled with the ease of mESC engineering and perturbation, makes this model system highly amenable to the study of multicellular self-organization. Defining the regulatory processes that drive axial elongation and cell differentiation in gastruloids could shed light on how similar events are achieved in the embryo; they may also provide a basis for the future engineering of user-defined tissue shapes and spatial arrangement of cell types.

Here, we seek to define how RTK-dependent signaling pathways control axial elongation and germ layer patterning by combining precise quantification of pathway activity and cellular responses with specific modulators of Ras/Erk and PI3K/Akt signaling. We first establish that the Erk and Akt pathways form highly reproducible posterior-to-anterior gradients that span ~500 µm, with Erk exhibiting an additional secondary peak of phosphorylation near the gastruloid midpoint. Quantification of signaling gradients in response to pathway inhibitors reveals unexpected regulatory complexity: namely, that PI3K/Akt is regulated by IGF1R independently of FGF signaling, and that the secondary Erk peak scales proportionally with overall gastruloid length. We further find that graded Erk and Akt activity control axial elongation via distinct downstream cellular processes: whereas both Erk and Akt signaling modulate overall gastruloid size, only the Erk gradient controls the expression of genes regulating gastruloid shape, tissue architecture and cell motility. Finally, we demonstrate that acute Erk activation is sufficient to specify two distinct cell fates in different regions of the gastruloid. Erk activation in the posterior half of the gastruloid drives all cells into a presomitic mesoderm (PSM) fate, whereas Erk activation in the anterior half converts this domain into precardiac mesoderm. Together, our data indicate that independent spatial gradients of Erk and Akt activity each play distinct functional roles in driving gastruloid morphogenesis and allocating cell fates.

#### **RESULTS**

# Mouse gastruloids possess posterior-to-anterior gradients of Erk and Akt activity

Despite extensive use of signaling inhibitors to perturb gastruloid development (Baillie-Johnson et al., 2015; Turner et al., 2016 preprint; van den Brink et al., 2020; Yaman and Ramanathan, 2023), few direct measurements of the Erk and Akt gradients have been performed. We thus first set out to quantify the spatial patterns of Erk and Akt activity during gastruloid elongation. We generated gastruloids using a Bra<sup>GFP</sup> mESC line (Fehling et al., 2003) in which GFP expression is driven from one of the endogenous *Bra* (*T*, brachyury) loci. Bra marks mesodermal cells in the posterior domain, providing information about germ-layer specification and serving as a useful fiducial pattern against which to compare the spatial distributions of additional signaling pathways and target genes. We grew gastruloids by sorting exactly 200 mESCs into each well of a round-bottom plate to reduce well-to-well variability,

followed by a standard protocol of media changes (Fig. 1A; Materials and Methods). This protocol resulted in aggregates with a major axis of approximately 1 mm at the end of day 5 (120 h); a small number (fewer than 5%) of the aggregates failed to elongate or formed multiple posterior domains. At 120 h, we fixed and stained gastruloids for either doubly phosphorylated Erk (ppErk) or phosphorylated Akt (pAkt), marking the active forms of both kinases. We then imaged the spatial distribution of the phosphorylated kinases, Bra<sup>GFP</sup>, and cell nuclei using DAPI. These experiments revealed that both ppErk and pAkt formed highamplitude, posterior-to-anterior signaling gradients, consistent with observations of graded Erk and Akt pathway activity in the mouse embryo (Dubrulle and Pourquié, 2004; Niwa et al., 2011) (Fig. 1B). Total Erk and Akt protein levels were approximately uniform along the major axis (Fig. S1A), indicating that the gastruloid does indeed contain a gradient in Erk/Akt pathway activity, not total protein levels. Although both kinases exhibited reproducible overall patterns, we observed substantial cell-to-cell heterogeneity in ppErk staining at the posterior pole, with significantly lower variability in the pAkt signal (Fig. 1B; Fig. S1B).

We next used an image-processing pipeline to quantify signaling patterns across many gastruloids (Fig. 1C; Materials and Methods). In brief, 100 µm confocal image stacks were collected for each gastruloid, and the mean pixel intensity was obtained for each axial position, generating an intensity profile along the major axis (Fig. 1C). Performing this quantification over many gastruloids revealed consistent long-range gradients in both Erk and Akt activity (Fig. 1D,E) that declined steeply from the posterior domain to approximately the midpoint along the major axis and exhibited a shallower decline in the anterior half of the gastruloid. In addition, we found that the Erk activity profile was non-monotonic, with a secondary ppErk peak located at approximately the gastruloid

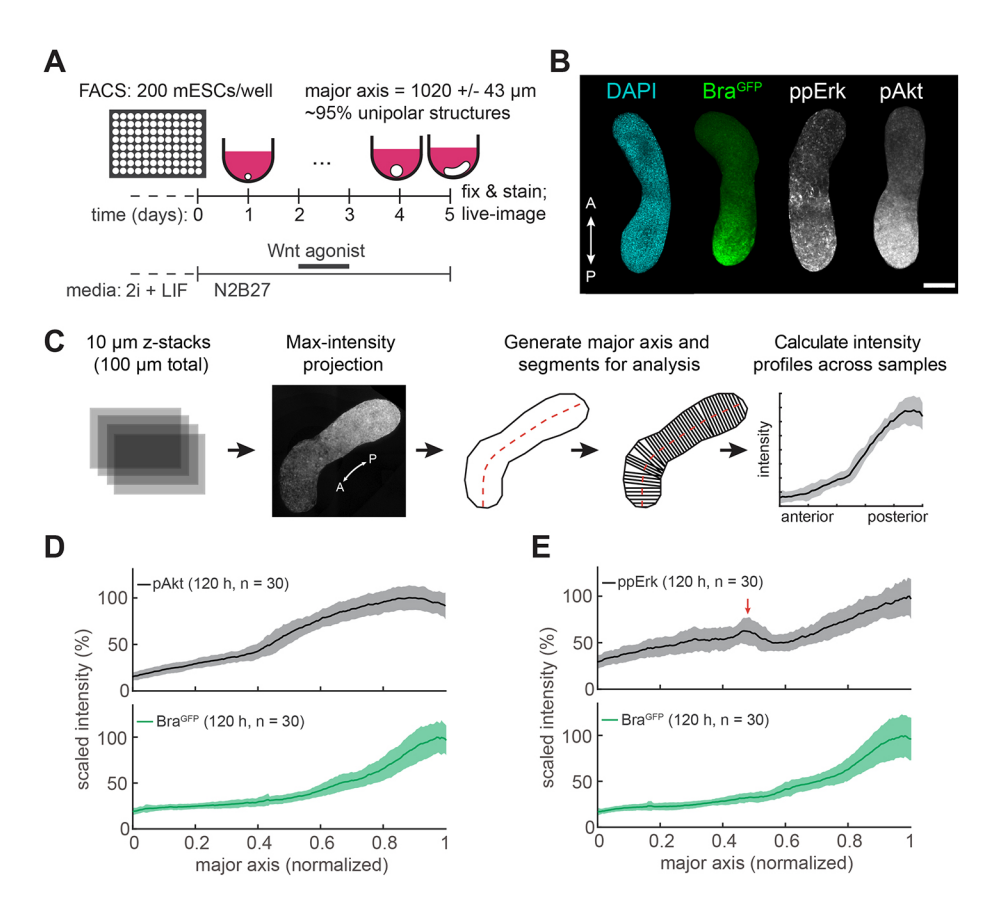


Fig. 1. Spatial domains of Erk and Akt signaling during gastruloid elongation.

(A) Schematic of gastruloid generation protocol. After seeding 200 cells per well, gastruloids are grown for 5 days, with addition of the Wnt agonist CHIR99021 from days 2 to 3. By the end of day 5, gastruloids elongate to ~1 mm in major axis length. FACS, fluorescence-activated cell sorting. (B) Representative gastruloid images showing nuclei (DAPI), brachyury reporter expression (BraGFP) and ppErk/pAkt gradients. Scale bar: 200 µm. (C) Gastruloid imaging and quantification pipeline. Z-stacks of fixed gastruloids are maximum-intensity projected and automatically segmented along their major axis to quantify A-P profiles. (D,E) Spatial profiles of pAkt or ppErk immunofluorescence staining and Bra<sup>GFP</sup> expression. The Erk secondary peak is indicated by the red arrow. Shaded error regions represent standard deviation (in all figures). For normalized major axes, 0=anterior and 1=posterior in all figures.

midpoint (Fig. 1E, red arrow). This is reminiscent of observations in the mouse embryo, where an oscillatory band of Erk activity marks the location of the posterior-most somite (Niwa et al., 2011). Automated analysis of single gastruloids (Materials and Methods; Fig. S1C) detected secondary ppErk peaks in 21 of the 30 gastruloids analyzed (Fig. S1D). These data suggest that the secondary ppErk peak is a somewhat variable phenotype, either only appearing in a subset of gastruloids or varying in amplitude in each gastruloid over time. Overall, these experiments reveal quantitatively reproducible, long-range, posterior-to-anterior patterns of Erk and Akt activity during gastruloid elongation.

## Kinase inhibitor treatments reveal functional roles for Erk/Akt signaling

How might these gradients of Erk and Akt activity depend upon upstream inputs, influence one another, and impact gastruloid development? To begin to address these questions, we treated gastruloids with small-molecule pathway inhibitors and monitored their effects on both signaling gradients and overall gastruloid size (Fig. 2A). Kinase inhibitors were added between days 4 and 5 of the protocol to examine their impact on axial elongation without disrupting earlier events, such as A-P axis establishment.

We found that FGFR inhibition (FGFRi) resulted in profound defects, with a ~40% reduction in major axis length and complete absence of BraGFP enrichment in the posterior domain, consistent with the loss of Bra expression in the primitive streak of  $Fgfr1^{-/-}$ embryos (Ciruna and Rossant, 2001) (Fig. 2B). A similar loss in Bra<sup>GFP</sup> expression was observed in response to MEK inhibitor (MEKi) treatment, with a partial reduction in gastruloid length that is consistent with other recent reports (Anand et al., 2023; Veenvliet et al., 2020; Yaman and Ramanathan, 2023; Yamanaka et al., 2023) (Fig. 2B). In contrast, PI3K (PI3Ki) and Akt (AKTi) inhibition resulted in smaller gastruloids with a shorter major axis, yet had no impact on the posterior expression of BraGFP (Fig. 2B). Akt inhibition closely phenocopied PI3K inhibition, suggesting that Akt is the major pathway node downstream of PI3K in this system. Taken together, these results indicate that gradients of Erk and Akt activity serve distinct functions, with Erk broadly regulating mesoderm-associated gene expression and elongation and Akt playing a more restricted role in elongation alone.

Canonically, RTK stimulation is thought to activate both Erk and Akt, which may then regulate one another via intracellular crosstalk (Mendoza et al., 2011). To test whether similar principles apply in this context, we next measured Erk and Akt signaling gradients in each inhibitor condition. We first verified that MEKi and AKTi treatment did indeed eliminate their respective Erk and Akt signaling gradients (Fig. S2A,B), validating that the inhibitors were functional at the concentrations used. PI3Ki treatment reduced but did not eliminate Akt phosphorylation (Fig. S2C), likely owing to high drug concentrations being required for complete inhibition. Nevertheless, we note that even this partial reduction phenocopied the more potent Akt inhibitor MK-2206 (Fig. 2B), suggesting that a high threshold of Akt activity is required for normal gastruloid morphogenesis. We further tested whether FGFR activity was required for both the Erk and Akt activity patterns. Notably, although FGFRi treatment abolished the Erk gradient (Fig. 2C), we found that the amplitude and spatial range of Akt phosphorylation was unaffected (Fig. S2D). Control of Akt by other RTKs, such as platelet-derived growth factor receptor (PDGFR) and insulin-like growth factor-1 receptor (IGF1R), is well documented in mouse models (Molotkov and Soriano, 2018; Riley et al., 2006), with IGF1R inhibition recently shown to

phenocopy Akt and PI3K inhibition in gastruloids (Suppinger et al., 2023). We found that whereas treatment with a PDGFR inhibitor (AG1296) had no impact on pAkt levels (Fig. S2E), treatment with an IGF1R inhibitor (OSI-906) led to a near-complete loss of pAkt across the entire major axis (Fig. 2D), marking IGF1R activity as the driver of the PI3K/Akt signaling gradient in mouse gastruloids.

We further tested for potential cross-talk between pathways by quantifying Erk patterning in Akt-inhibited gastruloids and vice versa. Just as in the case of FGFRi treatment, the Akt phosphorylation gradient was largely unaffected by the presence of a MEK inhibitor (Fig. 2E). The converse experiment – measuring Erk phosphorylation in the presence of an Akt or PI3K inhibitor – revealed an Erk pattern that was elevated relative to the DMSO-treated control at all normalized positions along the major axis (Fig. 2F; Fig. S2F). However, by plotting the level of Erk activity as a function of absolute position along the major axis, we found a close correspondence between the overall shape and magnitude of the gradients (Fig. 2G), indicating that PI3K/Akt signaling primarily influences gastruloid length and not Erk activity.

In contrast to the overall gradient shape, the absolute position of the secondary ppErk peak was substantially shifted in the smaller AKTi and PI3Ki gastruloids compared with untreated conditions (Fig. 2G, colored versus gray curves). These data led us to hypothesize that the position of this pattern feature may scale with overall gastruloid length. Indeed, measurement of the ppErk peak absolute position in individual gastruloids across all three treatment conditions revealed a tight linear scaling relationship ( $R_0^2=0.8$ ) with gastruloid length (Materials and Methods; Fig. 2H, left). No residual trend was observed when the normalized position of the secondary Erk peak was plotted against major axis length (Fig. 2H, right). Thus, although gastruloids harbor non-interacting, posterior-toanterior gradients in Erk and Akt activity, superimposed upon this profile is a secondary peak in Erk activity near the midpoint of the gastruloid, the position of which robustly scales with overall gastruloid length.

In sum, quantification of Erk and Akt signaling across inhibitor-treated gastruloids revealed distinct regulatory and functional relationships for both pathways. First, we find that both Erk and Akt activity are necessary for normal axis elongation, with inhibition of either signal reducing gastruloid length. Second, these posterior-to-anterior signaling gradients are established by at least two upstream inputs, with FGFR primarily driving the Erk activity pattern and IGF1R defining the Akt gradient. Finally, we demonstrate that although the Erk and Akt gradients are largely non-interacting, one feature of the Erk pattern – the position of an activity peak near the gastruloid midpoint – scales with overall gastruloid length.

# Cell proliferation and cell-cell adhesion are spatially patterned in elongating gastruloids

Our data so far reveal that perturbations to either Erk or Akt alter gastruloid size and shape (Fig. 2B). We next set out to characterize the cellular processes that drive gastruloid elongation to understand how they might be altered by Erk and Akt perturbation. We used differential interference contrast (DIC) microscopy to monitor tissue elongation in gastruloids, which were embedded in 50% Matrigel/50% N2B27 during the imaging period to provide mechanical stability and prevent large translational movements (van den Brink et al., 2020) (Fig. 3A; Materials and Methods). We then used particle image velocimetry (PIV) to quantify tissue flows during early and late phases of elongation (Materials and Methods).

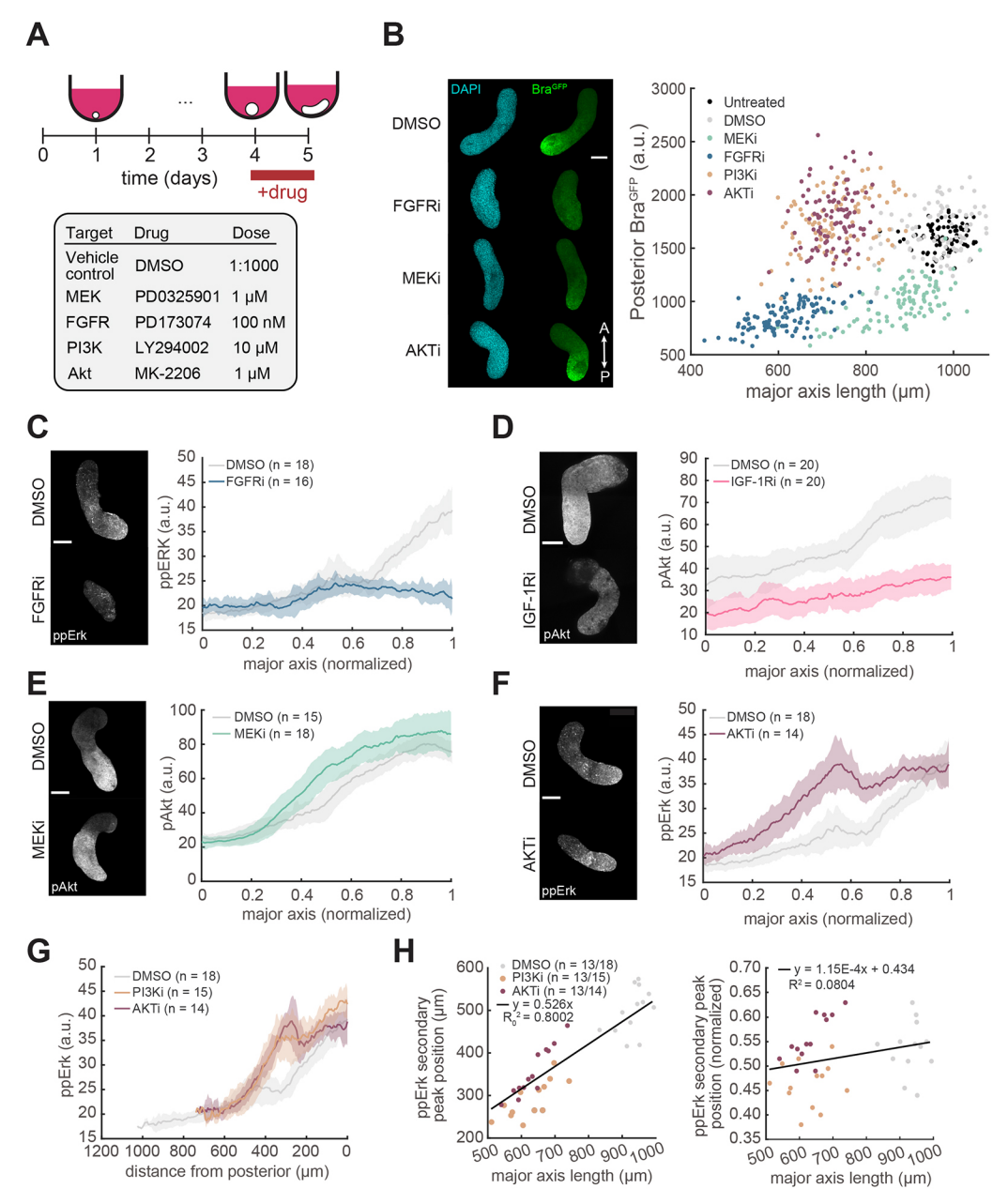


Fig. 2. Erk and Akt signaling are required for proper gastruloid elongation and are controlled by distinct upstream receptors. (A) Schematic of inhibitor treatment experiments. Inhibitors were administered during elongation (days 4-5). The working concentration for each inhibitor is indicated. (B) Left: Representative DAPI and Bra<sup>GFP</sup> images for DMSO, FGFRi, MEKi and AKTi treatments. Right: Quantification of major axis length and Bra<sup>GFP</sup> expression in the posterior 20% of the gastruloid after 24 h of inhibitor treatment, pooled from *n*=2 biological replicates. (C-F) Plots comparing either ppErk or pAkt spatial profiles between DMSO control and inhibitor-treated gastruloids, plotted on a normalized major axis where 0 is the anterior pole and 1 is the posterior pole. (G) Identical data to that shown in F but with ppErk intensity plotted as a function of absolute distance from the posterior pole. Note that the ppErk spatial profiles collapse onto the same curve with the exception of the secondary peak. (H) Left: Distance of the secondary ppErk peak from the anterior pole as a function of major axis length for all individual DMSO and PI3K/Akt inhibitor-treated gastruloids with a detectable secondary Erk peak. The *y*-intercept for the linear regression is fixed at zero. Right: Normalized position of the ppErk secondary peak as a function of major axis length. The 95% confidence interval for the slope of the linear regression is [-1.47×10<sup>-5</sup>, 2.46×10<sup>-4</sup>]. a.u., arbitrary units. Scale bars: 200 μm.

We confirmed that the Matrigel-embedding protocol preserved both tissue elongation as well as the posterior-to-anterior gradients in both ppErk and pAkt (Fig. S3A,B), demonstrating that these imaging conditions retain central features captured in our preceding experiments.

At the onset of elongation (96 h post-seeding), we observed the extrusion of a rigid cap-like domain (Fig. 3B, left; Movie 1), and endpoint imaging confirmed that only this domain expressed Bra<sup>GFP</sup>, marking it as the nascent posterior. PIV analysis revealed

that early during elongation the posterior and anterior portions of the tissue flowed apart at a rate of  $\sim\!10\text{--}15~\mu\text{m/h}$  (Fig. 3B, right; Movie 1). Later, between 109 and 120 h, the gastruloid exhibited steady, unidirectional elongation of the posterior domain (Fig. 3C, left; Movie 2). We performed PIV analysis to measure tissue flows relative to the elongating posterior; this analysis revealed that cells exited the posterior pole and moved anteriorly at a rate of  $\sim\!10\text{--}15~\mu\text{m/h}$  to drive overall outward displacement of a rigid posterior domain (Fig. 3C, right). An independent analysis

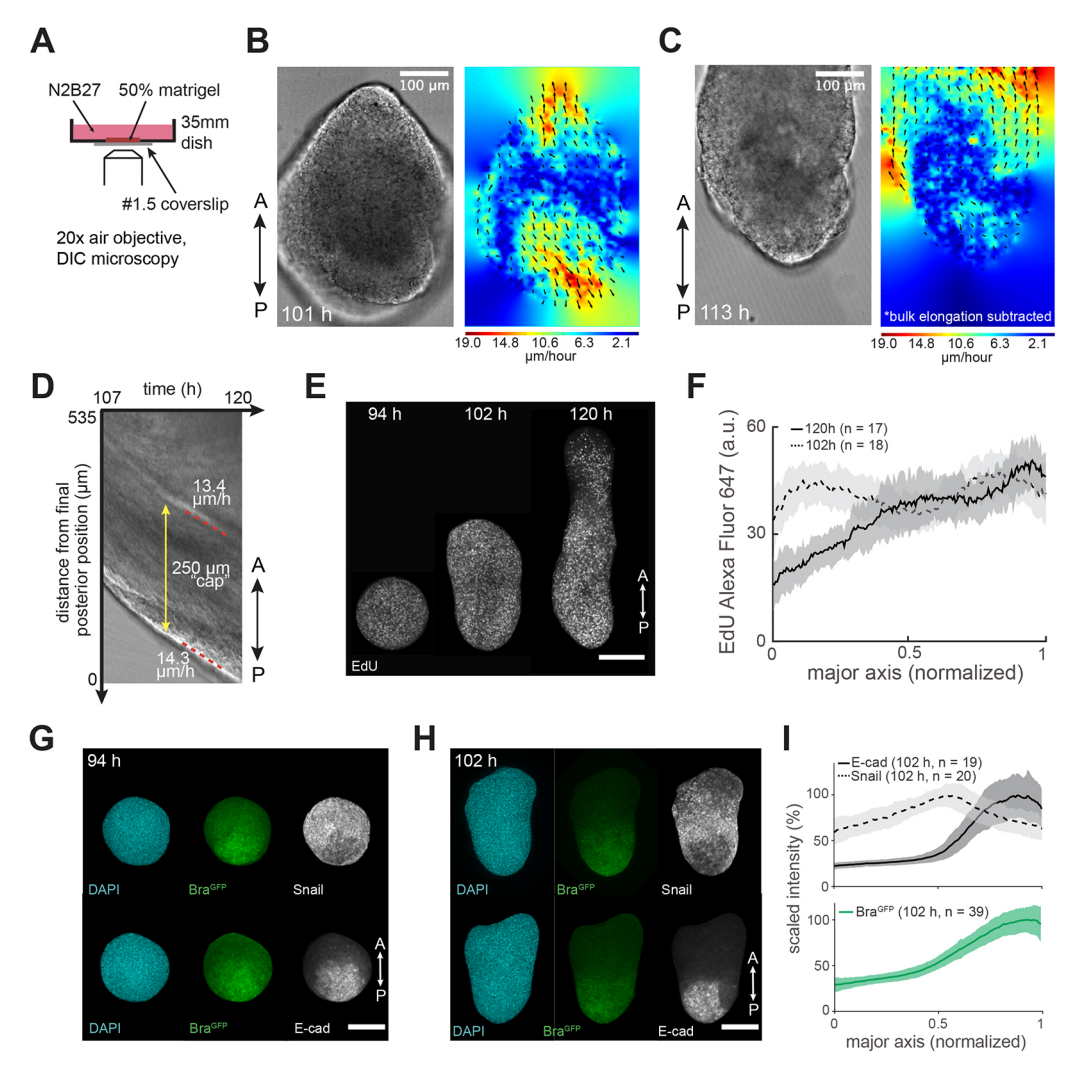


Fig. 3. Characterizing mechanisms of gastruloid elongation. (A) Schematic of the gastruloid live-imaging protocol. Gastruloids are placed in 50% Matrigel to limit lateral movement during live imaging. (B) Left: Frame from a live-imaging experiment at 101 h after aggregation, in which the gastruloid has begun to extrude a posterior cap. (B) Right: Mean velocity field generated from the previous hour of imaging using particle image velocimetry (PIV). Heat map represents magnitude of velocity vectors, with arrows indicating direction. (C) Left: Frame from a live-imaging experiment at 113 h after aggregation. Right: PIV analysis from the previous hour of the time lapse, with the outward movement of the posterior tip subtracted. (D) Kymograph generated from a vertical line along the gastruloid major axis using the sample shown in C. (E) Representative images of EdU staining at various time points during gastruloid elongation. (F) Quantification of EdU profiles for 102 h and 120 h gastruloids. (G,H) Sample images of DAPI, Bra<sup>GFP</sup>, Snail and E-cad at 94 h before physical elongation has begun (G), or 102 h, at the start of elongation (H). (I) Quantification of Bra<sup>GFP</sup>, Snail and E-cad spatial profiles at 102 h. The Bra<sup>GFP</sup> curve is aggregated for both staining treatments. a.u., arbitrary units. Scale bars: 200 μm (unless labeled otherwise).

of kymographs from the time-lapse movies revealed an elongation rate of  $\sim 13 \,\mu\text{m/h}$  (Fig. 3D), corroborating the results from the PIV analysis. These live-imaging data further pinpointed two processes that may be important for posterior elongation. First, we observed that elongation occurs without significant thinning near the posterior domain, necessitating a role for cell proliferation to maintain tissue width. Second, the extrusion of a rigid posterior cap from a more dynamic tissue domain suggests that differences in cell-cell adhesion and mechanical properties between these two tissue regions may play an important role. Such a difference in cellcell adhesion would be consistent with prior studies showing that the canonical adhesion regulator E-cadherin (E-cad; cadherin 1) is expressed specifically in the posterior domain of elongating gastruloids (Hashmi et al., 2022; van den Brink et al., 2014), although others have reported an E-cad-expressing core along the entire A-P axis of the gastruloid at 120 h (Vianello and Lutolf, 2020) preprint).

We next set out to confirm the local regulation of proliferation and cell-cell adhesion using more direct methods. We used a 5-ethynyl-2'-deoxyuridine (EdU) staining method to assess proliferation, which revealed that although proliferation was homogeneous in early gastruloids, a posterior-to-anterior gradient emerged as elongation proceeded (Fig. 3E,F). To characterize local differences in cell-cell adhesion, we stained for both E-cad and the epithelialmesenchymal transition-associated transcription factor Snail, factors for which expression often correlates with a tissue's material properties because of their impacts on cell movement and cell-cell contact strength (Barriga and Mayor, 2019). We found that E-cad expression is restricted to the presumptive posterior just prior to gastruloid elongation, with Snail+ cells surrounding this domain (Fig. 3G). Later during elongation, E-cad was expressed only at the posterior cap, whereas Snail protein was expressed in a band just anterior to this cap (Fig. 3H,I). Overall, our data support a model in which posterior elongation is driven by two distinct

processes: (1) localized cell proliferation at the posterior end to support elongation without tissue thinning, and (2) continued posterior displacement of a rigid E-cad<sup>+</sup> cap by newly added Snail<sup>+</sup> cells.

# Perturbing Akt signaling alters cell proliferation and gastruloid size

We next sought to characterize how the gradient of Akt signaling might modulate either proliferation or Snail/E-cad expression during elongation. We began by measuring Snail/E-cad protein levels in gastruloids treated for 24 h with AKTi or vehicle control. We found that AKTi treatment resulted in smaller gastruloids, but had little impact on the overall level of Snail or E-cad expression (Fig. 4A; Fig. S4A), supporting a model in which Akt signaling primarily acts to modulate cell proliferation rather than the expression of tissue architecture regulators. Interestingly, we again found evidence of a pattern that scales

with overall gastruloid size: the Snail peak was observed at  $\sim 60\%$  along the major axis in both control and AKTi conditions (Fig. 4A), and plotting the position of peak Snail expression as a function of major axis length revealed a tight proportionality between these quantities (Fig. 4B). FGF/Erk signaling is known to regulate Snail expression (Ciruna and Rossant, 2001), and our similar observations for the secondary ppErk peak suggests that these scaling relationships may be causally linked.

To test further for a link between Akt signaling and local cell proliferation, we developed a protocol to pool and dissociate known numbers of gastruloids and measure both the total and live cell counts per gastruloid (Materials and Methods; Fig. 4C, top). We found that AKTi treatment led to a ~30% reduction in the number of live cells per gastruloid at 120 h, from an average of 62,000 cells per gastruloid in the vehicle control to 43,000 cells per gastruloid upon AKTi treatment (Fig. 4C, bottom). A reduced live cell count could, in principle, arise from either a decrease in cell proliferation or an

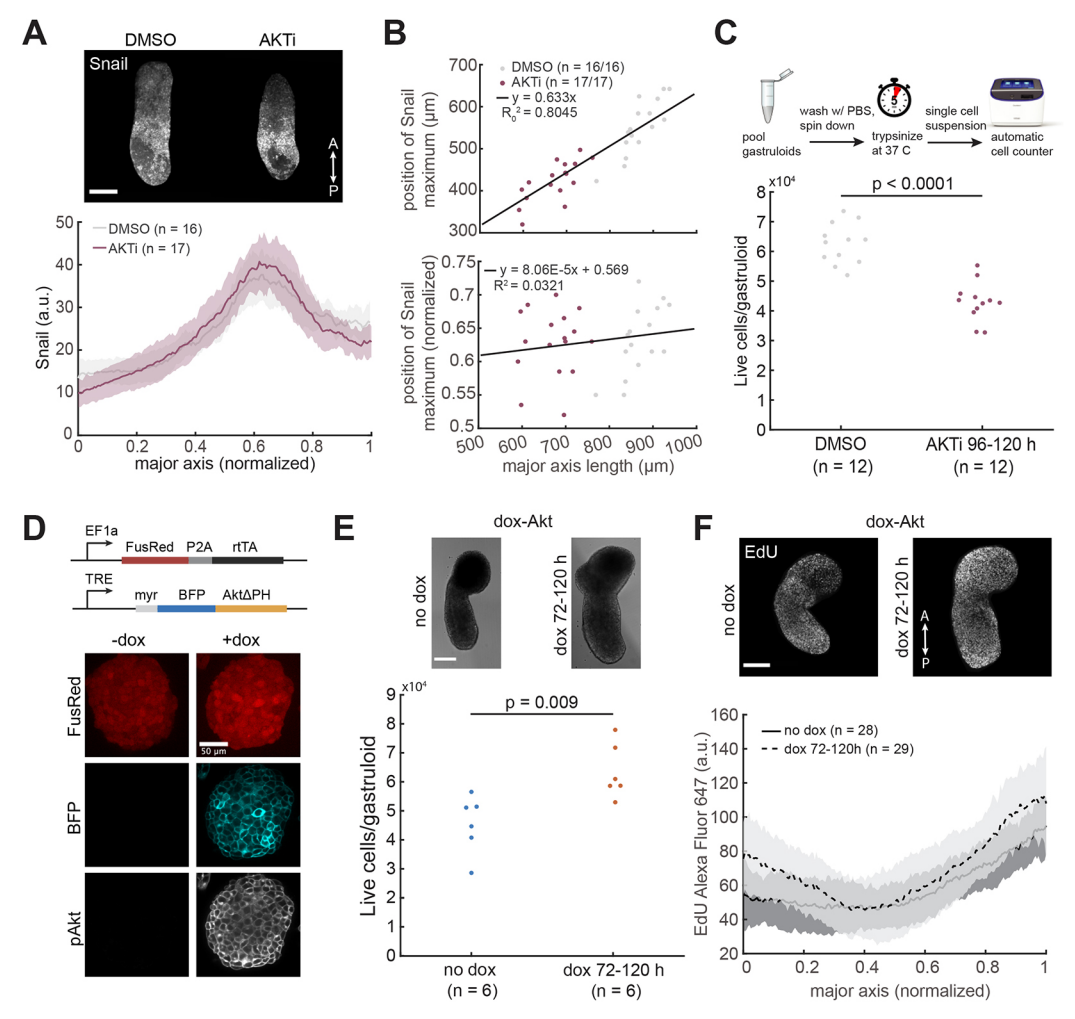


**Fig. 4. PI3K/Akt signaling modulates proliferation along the gastruloid major axis.** (A) Spatial profile of Snail expression after DMSO or AKTi treatment. (B) Top: Distance of the Snail peak from the anterior pole as a function of major axis length for all DMSO and AKTi-treated gastruloids. The *y*-intercept for the linear regression is fixed at zero. Bottom: Normalized position of the Snail peak as a function of major axis length. The 95% confidence interval for the slope of the linear regression is [–8.16×10<sup>–5</sup>, 2.43×10<sup>–4</sup>]. (C) Live cells per gastruloid for Akt inhibition compared with vehicle control. Each data point represents the average cell count per gastruloid found after pooling five gastruloids. Data are aggregated from *n*=3 biological replicates. (D) Schematic of dox-Akt expression system and representative images for FusionRed, BFP and pAkt in the absence or presence of 1 μg/ml doxycycline (dox). (E) Live cells per gastruloid after treatment of dox-Akt gastruloids with 1 μg/ml doxycycline from 72 to 120 h, compared with a doxycycline-free control. Each data point represents the average cell count per gastruloid found from pooling ten individual gastruloids. Data are aggregated from *n*=3 biological replicates. (F) EdU staining after treatment of dox-Akt gastruloids with 1 μg/ml doxycycline from 72 to 120 h, compared with a doxycycline-free control. *P*-values were calculated by two-tailed *t*-test. a.u., arbitrary units. Scale bars: 200 μm (unless labeled otherwise).

increase in cell death, but Trypan Blue staining revealed only a minor decrease in the proportion of live cells after AKTi treatment (Fig. S4B,C). Akt inhibition thus appears to decrease gastruloid size primarily by suppressing cell proliferation.

We next set out to perform the converse experiment: testing whether global Akt hyperactivation might induce hyper-proliferation and increased gastruloid growth. As an initial test of this model, we treated gastruloids with platelet-derived growth factor (PDGF), a known activator of Akt signaling in a wide variety of developmental contexts (Van Stry et al., 2005; Yang et al., 2008). We confirmed that, in gastruloids, PDGF treatment leads to an increase in pAkt levels, most notably in the anterior domain where Akt activity is normally absent (Fig. S4D). In conjunction with this expanded profile of Akt signaling, we observed high levels of EdU incorporation in the anterior domains of elongating gastruloids (Fig. S4E), indicative of a shift from local to global cell proliferation, as well as significant gastruloid enlargement in response to PDGF treatment (Fig. S3F).

Receptor-level activation using PDGF activates a number of downstream pathways, including PI3K/Akt, Ras/Erk, PLCy and JAK/STAT signaling (Van Stry et al., 2005). We thus sought an alternative method to more specifically isolate Akt for activation. Inspired by chemogenetic and optogenetic tools demonstrating that Akt membrane localization is sufficient to drive its activation (Ng et al., 2008; Wang et al., 2020), we engineered a stable mESC cell line with doxycycline-inducible expression of blue fluorescent protein (BFP)-tagged, membrane-localized Akt, hereafter referred to as dox-Akt cells (Fig. 4D). We confirmed that 24 h treatment with 1 μg/ml doxycycline drove a dramatic increase in both BFP expression and Akt phosphorylation in dox-Akt cells (Fig. 4D), demonstrating that this cell line can indeed be used to produce high levels of Akt activity robustly in response to doxycycline treatment. We found that when dox-Akt gastruloids were exposed to 1 µg/ml of doxycycline from 72 to 120 h, the aggregates were wider and longer (Fig. S4G) and contained a greater number of cells (Fig. 4E) without a change in gastruloid aspect ratio (Fig. S4H) or cell viability (Fig. S4I). Akt hyperactivation also drove a minor increase in EdU incorporation at most positions along the gastruloid major axis (Fig. 4F). Finally, just as in the case of AKTi treatment, the domains of Snail and E-cad expression were unperturbed in dox-Akt gastruloids (Fig. S4J,L). Taken together, these experiments demonstrate that an Akt signaling gradient locally regulates cell proliferation to support the posterior domain's growth during gastruloid elongation.

# Perturbing Erk activity alters Snail/E-cad expression patterns and gastruloid shape

How does Erk signaling affect the cellular processes associated with gastruloid morphogenesis? In contrast to our previous observations with Akt inhibition (Fig. 4A; Fig. S4A), Snail expression was reduced in MEKi-treated gastruloids (Fig. 5A) and replaced by an extended domain of E-cad expression out to  $\sim$ 50% along the gastruloid major axis (Fig. 5B). These changes in gene expression were also reflected in the tissue flows during elongation (Movie 3): although elongation was still possible, the posterior cap became longer and more pointed over time (Fig. S5B,C), consistent with expansion of the E-cad domain and reminiscent of the phenotype of Fgf4/8 conditional knockout mouse embryos (Boulet and Capecchi, 2012). MEKi-treated gastruloids also had a lower average number of cells than the vehicle control, but the impact on proliferation was less pronounced than upon Akt inhibition (Fig. S5A). Thus, unlike Akt, Erk activity primarily impacts the patterned expression of

genes associated with cell-cell adhesion during gastruloid elongation, altering tissue shape.

We also engineered gastruloids in which Erk signaling could be globally activated using a doxycycline-inducible, BFP-tagged, membrane-localized activator of Ras (dox-SOScat) (Fig. 5C), analogous to the dox-Akt system described above. SOS is a guanine nucleotide exchange factor that activates Ras upon membrane recruitment, and localizing the catalytic domain of SOS (SOS<sup>cat</sup>) to the membrane is sufficient to potently activate the Ras/Erk signaling cascade (Gureasko et al., 2008; Toettcher et al., 2013). Treatment of clonal dox-SOS<sup>cat</sup> mESCs with 1 µg/ml doxycycline for 24 h resulted in elevated BFP expression and ppErk levels, validating the efficacy of this approach (Fig. 5C). Although doxycycline treatment activated Erk in all cells, we observed cell-to-cell differences in ppErk that were not well correlated with BFP expression levels, suggesting that additional cell state variables may fine-tune sensitivity to SOS<sup>cat</sup> expression and membrane localization. Treating dox-SOS<sup>cat</sup> gastruloids with doxycycline from 96 to 120 h resulted in a profound morphological change: the resulting gastruloids were nearly spherical, with a dramatically reduced aspect ratio (Fig. 5D). Despite this change in shape, dox-SOS<sup>cat</sup> gastruloids contained more cells (Fig. 5E), confirming Ras/Erk signaling as a proliferative signal in this context. We hypothesized that the near-isotropic growth of dox-SOS<sup>cat</sup> gastruloids was again due to a loss of polarized gene expression, disrupting local control over cell mechanics. Indeed, staining for Snail and E-cad in dox-SOScat gastruloids that were induced with doxycycline from 96 to 120 h revealed global expression of Snail and a near-complete loss of E-cad expression (Fig. 5F,G). Taken together, these observations implicate Erk signaling as a potent regulator of gastruloid shape, at least in part by modulating the balance between Snail<sup>+</sup> and E-cad<sup>+</sup> tissue domains.

### Erk signaling drives PSM and precardiac mesoderm fates

Gastruloid development is not limited to posterior elongation, but rather involves a multitude of coordinated, spatially localized differentiation events, many of which are known to depend on RTK activity. In the mouse embryo, FGF signaling has been shown to play a central role in the differentiation of posterior-localized NMPs to either neural or mesodermal lineage. Loss of FGF signaling is associated with the formation of ectopic neural tubes (Boulet and Capecchi, 2012; Ciruna and Rossant, 2001; Ciruna et al., 1997), whereas Raldh2 (Aldh1a2)<sup>-/-</sup> mouse embryos harboring an expanded domain of posterior Fgf gene expression exhibit a significant enlargement of the PSM population (Cunningham et al., 2015). At more anterior positions, FGF signaling is crucial for the specification of cardiac mesoderm, with  $Fgf8^{-/-}$  mouse embryos failing to form a heart by E8.5 (Sun et al., 1999). FGFb and VEGF are canonical pro-cardiac growth factors (Kattman et al., 2006) and, in conjunction with ascorbic acid, were recently used to induce cardiogenesis in a gastruloid system (Rossi et al., 2021). Although much has been established regarding the necessity and sufficiency of receptor-level RTK activity in driving these specific differentiation events in the mouse embryo, it remains largely unexplored how specific intracellular pathways are contributing to these decisions. We thus set out to utilize our Erk and Akt inhibition and hyperactivation tools to determine the direct roles of these pathways in driving RTK-associated cell differentiation.

We first established a baseline for the spatial distribution of all three germ layers and specific anterior/posterior mesodermal subpopulations by staining for canonical transcription factors associated with each cell fate. The gastruloid at day 5 serves as an approximation of the E8.5 mouse embryo (Beccari et al., 2018), and

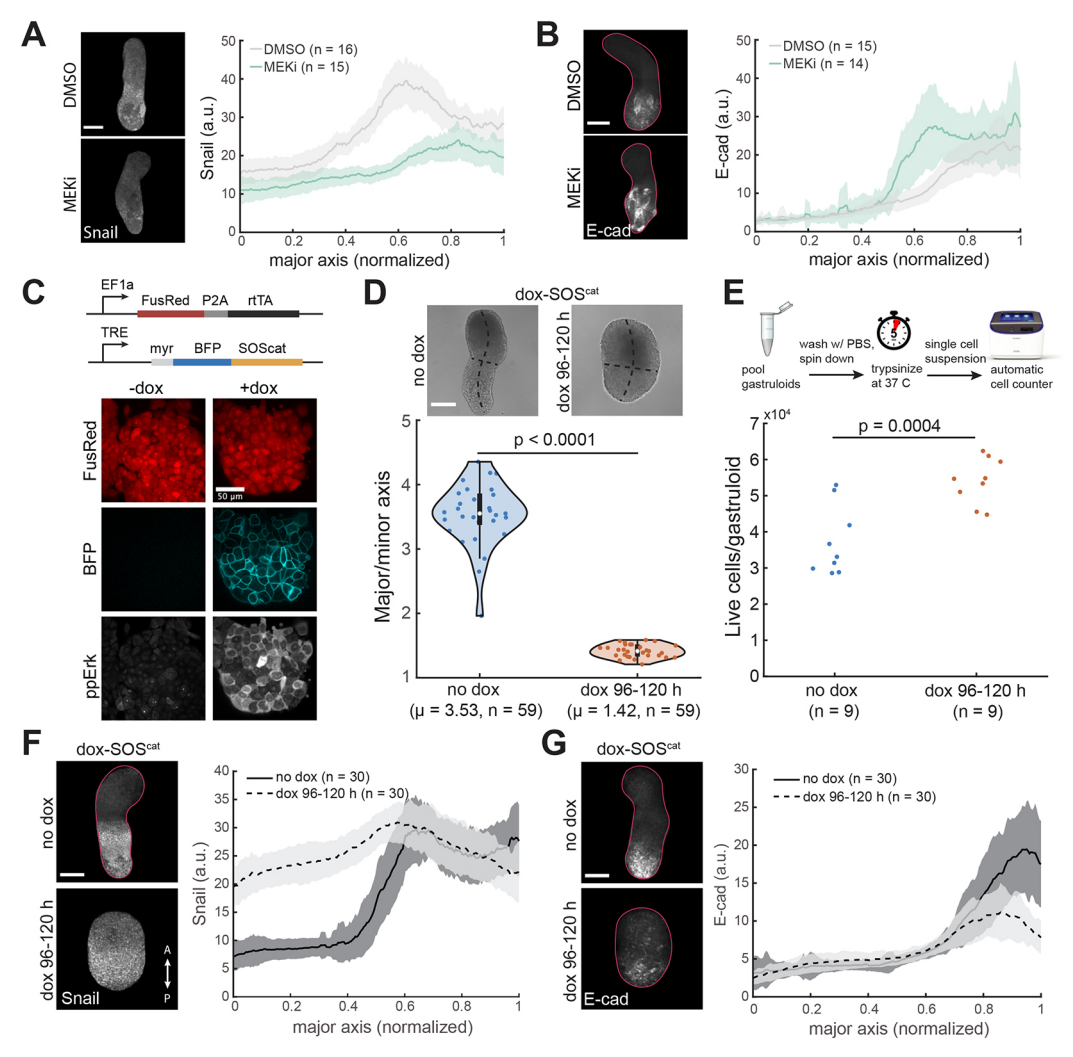


**Fig. 5. Ras/Erk signaling is necessary and sufficient for Snail expression.** (A,B) Spatial profiles of Snail and E-cad expression after MEK inhibition, compared with vehicle control. (C) Schematic of dox-SOS<sup>cat</sup> expression system and representative images for FusionRed, BFP and ppErk in the absence or presence of 1 μg/ml doxycycline (dox). (D) Major/minor aspect ratio for dox-SOS<sup>cat</sup> gastruloids treated with 1 μg/ml doxycycline from 96 to 120 h, compared with a doxycycline-free control. (E) Live cells per gastruloid after treatment of dox-SOS<sup>cat</sup> gastruloids with 1 μg/ml doxycycline from 96 to 120 h, compared with a doxycycline-free control. Each data point represents the average cell count per gastruloid found from pooling ten individual gastruloids. Data from *n*=3 biological replicates. (F,G) Spatial profiles of Snail and E-cad for dox-SOS<sup>cat</sup> gastruloids treated with 1 μg/ml doxycycline from 96 to 120 h, compared with a doxycycline-free control. *P*-values were calculated by two-tailed *t*-test. a.u., arbitrary units. Scale bars: 200 μm (unless labeled otherwise).

contains a complex spatial arrangement of cell types (Fig. 6A). Along the dorsal side of the embryo, a population of SOX2expressing cells marks the neuroectoderm of the developing neural tube and neural plate, with co-expression of SOX2 and brachyury in the anterior primitive streak marking the NMPs (Ellis et al., 2004; Garriock et al., 2015; Wood and Episkopou, 1999). On the ventral side of the embryo, SOX17 marks the definitive endoderm, which goes on to establish the primitive gut tube (Engert et al., 2009; Kanai-Azuma et al., 2002; Matsui et al., 2006). The mesoderm of the E8.5 embryo has differentiated into transcriptionally diverse subpopulations, including TBX6-expressing PSM at the posterior pole and GATA6-expressing precardiac mesoderm in an anterior domain (Chapman et al., 1996; Morrisey et al., 1996). At 120 h, gastruloids faithfully recapitulate a subset of this germ layer organization (Fig. 6B). In the posterior region of the gastruloid, we observed a discrete population of TBX6<sup>+</sup> PSM cells and a complementary domain of SOX2<sup>+</sup> neuroectoderm/NMP cells (Fig. 6B, top). We found small, variable populations of SOX17<sup>+</sup> definitive endoderm cells distributed along the gastruloid A-P axis,

with the highest-expressing cells also positive for GATA6 (Fig. 6B, bottom). This contrasts with previous reports of a significant population of GATA6<sup>+</sup> cells at the anterior pole of the gastruloid at this stage (Beccari et al., 2018). This discrepancy may be the result of differences in the differentiation state of the initial stem cell population, as Beccari et al. grew mESCs in the absence of 2i-containing media prior to gastruloid seeding.

We next sought to establish the direct role of either Erk or Akt signaling in driving cell-fate specification, in particular the allocation of PSM from NMPs and the formation of a precardiac mesoderm population. We found that MEKi treatment from 96 to 120 h resulted in a complete loss of TBX6 protein without substantially altering the posterior SOX2 expression domain (Fig. 6C,D). This is in contrast to AKTi treatment, which produced shorter gastruloids but otherwise retained the SOX2 and TBX6 expression patterns of untreated gastruloids (Fig. S6A). Finally, GATA6 and SOX17 expression levels remained low and unchanged upon either MEKi or AKTi treatment, indicating little change to endoderm differentiation under these conditions (Fig. S6B). Overall, these results are consistent with

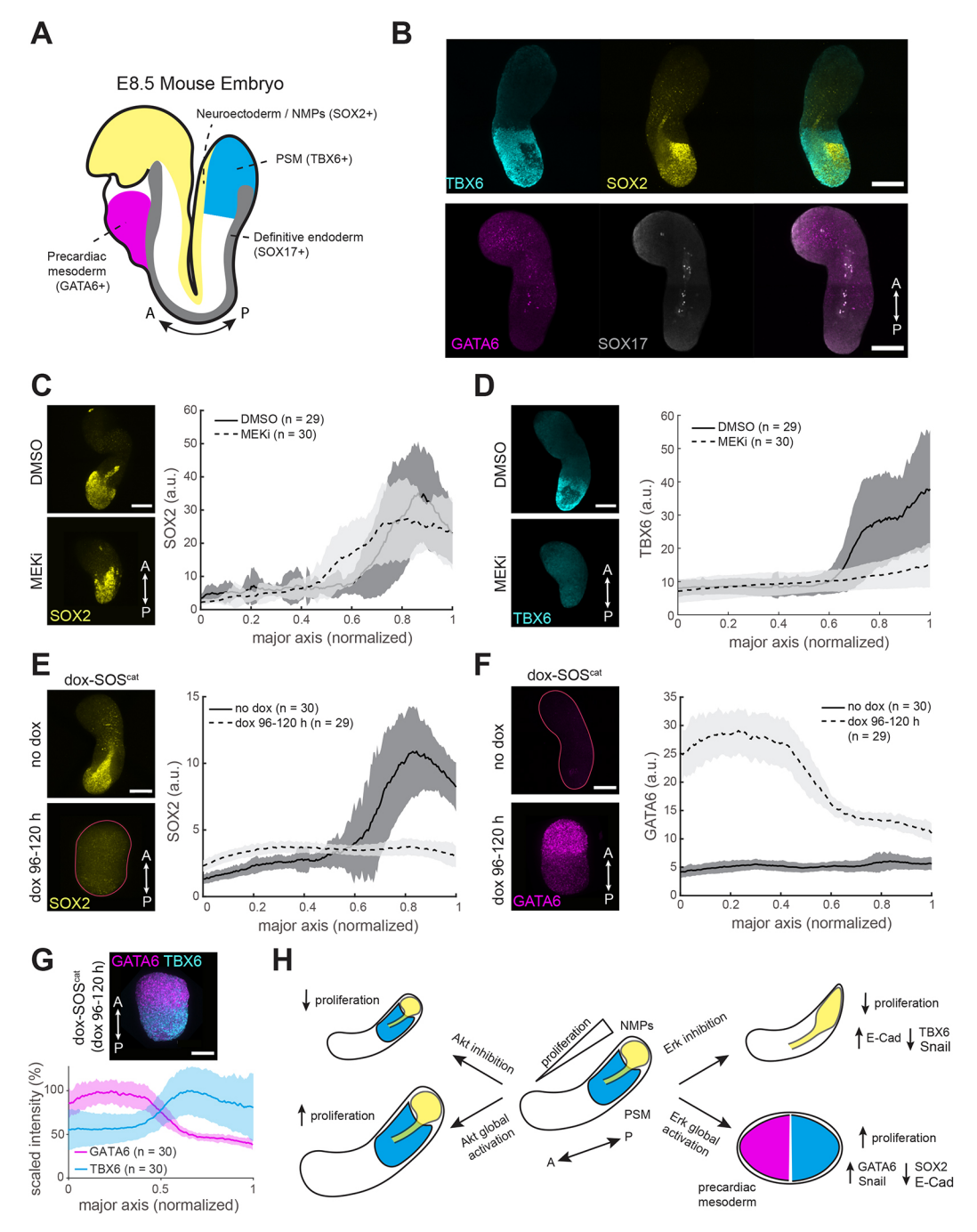


**Fig. 6. Ras/Erk signaling controls distinct cell fates depending on A-P axis location.** (A) Schematic of selected cell types and corresponding fate markers in the E8.5 mouse embryo. (B) Representative images of GATA6, SOX17, SOX2 and TBX6 expression in a wild-type 120 h gastruloid. (C,D) Spatial profiles of SOX2 and TBX6 expression after MEK inhibition, compared with vehicle control. (E,F) Spatial profiles of SOX2 and GATA6 for dox-SOS<sup>cat</sup> gastruloids treated with 1 μg/ml doxycycline from 96 to 120 h, compared with a doxycycline-free control. (G) Comparison of spatial profiles of GATA6 and TBX6 in dox-SOS<sup>cat</sup> gastruloids treated with 1 μg/ml doxycycline from 96 to 120 h. (H) Summary of Ras/Erk and Pl3K/Akt signaling perturbations and their resultant phenotypes. Akt inhibition or global activation leads to an increase or decrease in cell proliferation, respectively, thus impacting gastruloid size. Erk inhibition decreases proliferation and leads to an expansion of the E-cad domain at the expense of Snail and TBX6 expression. Erk global activation, by comparison, drives greater proliferation and generates a Snail+ aggregate with two distinct mesodermal poles. a.u., arbitrary units. Scale bars: 200 μm.

the necessity of Erk but not Akt signaling for PSM differentiation from NMPs in the posterior domain of the gastruloid, suggesting that the failure to specify PSM in FGF loss-of-function mouse embryos can be explained solely by reduced Ras/Erk activity under these conditions.

We further tested whether acute Akt or Erk activation could also be sufficient to alter cell-fate outcomes using our doxycycline-inducible cell lines. Whereas Akt hyperactivation had minimal impact on germ layer markers (Fig. S6C), Erk hyperactivation drove profound changes in cell identity. Gastruloids grown from dox-SOS<sup>cat</sup> cells and induced with dox from 96 to 120 h exhibited a complete loss of SOX2 expression (Fig. 6E) as well as the formation of a posterior hemisphere that was entirely TBX6/BRA positive (Fig. S6D). A distinct response was observed in the anterior domain, where Erk

activation drove dramatic upregulation of GATA6 (Fig. 6F). Simultaneously staining for both GATA6 and TBX6 revealed roughly equal partitioning between these two populations (Fig. 6G), suggesting near-complete conversion of the gastruloid to a combination of precardiac and presomitic mesoderm. This treatment did not appear to impact endoderm specification, as a similarly low number of SOX17<sup>+</sup> cells was observed in both cases (Fig. S6D). In summary, these findings reveal that, in addition to its roles regulating proliferation and morphogenesis, Erk signaling is also sufficient to simultaneously trigger two distinct differentiation events – the conversion of NMPs to PSM and the specification of GATA6<sup>+</sup> precardiac mesoderm – in non-overlapping spatial domains.

#### **DISCUSSION**

Localized RTK signaling plays conserved, recurring roles throughout embryogenesis. This receptor-level activation is complex and can interface with many different intracellular pathways, depending on cell type and context, with the specific functions of individual pathways in many cases still unknown. Here, we investigate the spatial patterning of the activity of two RTK-associated signaling pathways, Ras/Erk and PI3K/Akt, and their role in driving gastruloid morphogenesis and cell-fate specification. We find that both pathways form reproducible posterior-to-anterior activity gradients, reflecting localized activity that has also been observed in the mouse embryo. Unexpectedly, treatment with pathway inhibitors reveals that these activity patterns are generated independently by two upstream RTKs, with Erk controlled by FGFR and Akt controlled by IGF1R, and that there is minimal cross-talk between the two pathways. Finally, we find that these two signaling pathways control overlapping but distinct aspects of gastruloid development. Whereas Akt activity solely modulates gastruloid size by controlling proliferation along the A-P axis, Erk signaling regulates multiple outputs, including proliferation, cell-cell adhesion, gastruloid shape and the specification of distinct cell fates. We further find that appropriate spatial patterning of each pathway is crucial, as global stimulation of Akt is sufficient to drive hyperproliferation in the gastruloid's anterior domain, whereas ectopic Erk activation can drive multiple differentiation decisions at different spatial positions, dramatically altering gastruloid shape and the allocation of cell fates.

One surprising finding from our quantification of signaling and gene expression patterns is that some Erk-associated features scale with total gastruloid length. We observe that a peak of Erk activity and its downstream effector Snail appear at precise relative positions within the gastruloid, regardless of the gastruloid's total size. The position of the Erk activity peak may correspond to the gastruloid's equivalent of the last somite in the mouse embryo, which is marked by a band of oscillatory Erk activity (Niwa et al., 2011). Sizeinvariant scaling of this ppErk peak may be a mechanism by which the system ensures the proper segmentation of the body plan across embryos of various sizes. A recent preprint has presented compelling evidence that many other downstream gene expression patterns, including the SOX2 and brachyury expression profiles, scale with overall gastruloid length (Merle et al., 2023 preprint). Our data reveal that scaling can be observed even in the uppermost patterns of signaling pathway activity and further support the idea that mammalian multicellular aggregates possess intrinsic mechanisms to robustly generate signaling and gene expression patterns in response to significant variation in aggregate size. The mechanism by which size scaling is achieved remains unknown and is a rich domain for future study.

Many studies of mammalian development use loss-of-function mutants or pharmacological inhibitors of a signaling protein to assess its necessity in driving a particular developmental outcome. Studies that address the converse – whether a certain signal is sufficient – have often been limited to receptor-level control, for example by using exogenous ligand addition or knockout of a negative regulator of endogenous ligand production (Cunningham et al., 2015; Rossi et al., 2021). However, receptor-level activation triggers numerous downstream pathways and prolonged stimulation may be susceptible to negative feedback, making it difficult to connect developmental phenotypes to a single intracellular pathway of interest. Here, we sought to bypass these additional complexities using acutely inducible activators of specific signaling pathways (dox-Akt and dox-SOScat). By specifically activating just one intracellular pathway at a time, we found that PI3K/Akt signaling is sufficient to induce proliferative activity at anterior positions in the gastruloid that are not normally mitotically active, leading to expansion of these domains and altered gastruloid size. We also revealed that Ras/Erk hyperactivation was sufficient to alter patterns of gene expression globally. These gene expression changes had major consequences on gastruloid shape, at least in part by altering domains of E-cad and Snail expression. This treatment also affected cells' differentiation state by converting posterior NMPs to TBX6<sup>+</sup> PSM, and by generating GATA6<sup>+</sup> precardiac mesoderm in the gastruloid's anterior half.

Our results suggest that a single pathway (Erk signaling) is sufficient to drive differentiation of two distinct mesodermal lineages at the same time during mammalian development. It remains unknown whether these fate decisions depend on differences in the intrinsic potential of anterior and posterior cell populations, or if they rely on exposure to additional anterior- or posterior-localized signaling cues. These profound changes to cell fate driven by Erk hyperactivation were broadly reminiscent of the early development of cardiac gastruloids (Rossi et al., 2021), which also contain distinct domains of brachyury and GATA6 expression after having been exposed to a cocktail of cardiogenic factors that included two RTK ligands (bFGF, VEGF and ascorbic acid).

A closer examination of Erk-dependent fates at the posterior domain also presents an apparent contradiction: if Erk signaling is normally high at the posterior pole (Fig. 1), and Erk activity is sufficient to convert NMPs to PSM (Fig. 6), then how is an NMP population maintained in the posterior during normal gastruloid development? One possible explanation can be found in the substantial heterogeneity in ppErk levels amongst posterior cells (Fig. S1B). It is possible that high-Erk and low-Erk cells co-exist in the posterior and correspond to PSM or NMP/neuroectoderm fates, respectively. A careful study of the timing of Ras/Erk activation in single cells using live-cell signaling reporters (Regot et al., 2014), in conjunction with live readouts of cell fate acquisition, may provide further information regarding the level and duration of Erk signaling required to drive differentiation of these cells. The substantial heterogeneity in posterior ppErk staining also suggests that these cells are differentially sensitive to extracellular FGF, presenting a compelling domain for future study.

A quantitative atlas of developmental signaling can serve many useful functions. We have shown here that quantification of signaling gradients, their interactions, and their downstream effects can reveal insights into the regulation of growth and patterning in multicellular systems. Moreover, the characterization we have performed here is also a prerequisite for 'rewriting' patterns using the tools of optogenetics or synthetic biology. We must have an accurate understanding of where and when a particular signaling pattern is active, and what role it plays, before we can predict how an alternative pattern might drive different outcomes. Many optogenetic

tools are already available for controlling Erk, Akt and RTK activity in cells and organisms (Grusch et al., 2014; Kim et al., 2014; Toettcher et al., 2013; Wang et al., 2020). We anticipate that the data presented here may enable the experimentalist to explore the rules of morphogenesis and cell fate allocation through delivery of customized, user-defined patterning cues.

#### **MATERIALS AND METHODS**

#### **Plasmids and cloning**

All constructs were cloned into a PiggyBac plasmid (System Biosciences). Linear DNA fragments were amplified via PCR using CloneAmp HiFi PCR premix (Takara Bio, 639298). PCR products were cut from agarose gels and purified using the Nucleospin gel purification kit (Takara Bio, 740609). Final plasmids were constructed using In-Fusion HD (Takara Bio, 638910) and amplified in Stellar chemically competent *Escherichia coli* (Takara Bio, 636763). DNA was extracted by miniprep (QIAGEN, 27104). All plasmid verification was performed by Sanger sequencing (GENEWIZ) or nanopore sequencing (Plasmidsaurus). The dox-Akt and dox-SOScat plasmids can be obtained on Addgene (plasmid #207328 and #207329, respectively). The *Akt1* gene (without the pleckstrin homology domain) was codon optimized for *Mus musculus* and was ordered as a gBlock (Integrated DNA Technologies). The SOScat gene was cloned from existing plasmids and can be obtained on Addgene (plasmid #86439).

#### **Routine cell culture**

The E14TG2a Bra<sup>GFP</sup> cell line was a gift from Dr Alfonso Martinez Arias (Cambridge University, UK). The dox-Akt and dox-SOS<sup>cat</sup> cell lines were generated using wild-type E14TG2a cells (recently purchased from ATCC). All other experiments were carried out using the E14TG2a Bra<sup>GFP</sup> cell line. Cell lines were routinely tested for *Mycoplasma* contamination using a PCR-based universal *Mycoplasma* detection kit (ATCC, 30-1012K).

All mESCs were grown in 2i+ LIF media. This consists of a base media of GMEM (Millipore Sigma, G6148) with 10% ESC qualified fetal bovine serum (R&D Systems, S10250), 1:100 GlutaMAX (Gibco, 35050-061), 1:100 MEM non-essential amino acids (Gibco, 11140-050), 1 mM sodium pyruvate (Gibco, 11360-070) and 100  $\mu$ M 2-mercaptoethanol (Gibco, 21985-023). For a working stock of 2i+ LIF media, this base media was supplemented with 1:100 penicillin/streptomycin solution (Pen Strep; Gibco, 15140-122),  $10^3$  units/ml ESGRO recombinant mouse LIF protein (Millipore Sigma, ESG1107), 2  $\mu$ M PD0325901 (Tocris, 4192) and 3  $\mu$ M CHIR99021 (Tocris, 4423).

mESCs were grown in filter-capped tissue culture flasks. These flasks were treated with a 0.1% gelatin solution in water (Millipore Sigma, ES-006-B) for 30 min prior to plating cells. Cells were passaged every 48 h. To passage, media was aspirated from the flask and cells were washed with pre-warmed DPBS (–)Calcium (–)Magnesium (Gibco, 14190144). The DPBS was aspirated and cells were treated with pre-warmed TrypLE Express Enzyme, enough to cover the bottom of the flask evenly (Gibco, 12605028). Cells were incubated in trypsin at 37°C for 5 min, then 2i+ LIF media was added and cells were triturated to form a single-cell suspension. Cells were centrifuged at 135 g for 5 min, then the supernatant was aspirated and the cell pellet was resuspended in 2i+ LIF media. The 0.1% gelatin solution was aspirated from the flask, and cells were plated at the desired density (typically a 1:5 to 1:10 dilution).

#### **Cell line generation**

Clonal transgenic cell lines were generated via transfection and PiggyBac genomic integration. Cells were plated 24 h before transfection in a cell-culture treated 6-well plate (Fisher Scientific, 14-832-11). To transfect, 2000 ng of the PiggyBac vector plasmid and 500 ng of the PiggyBac transposase plasmid (System Biosciences, PB210PA-1) were mixed in 125 µl Opti-MEM (Gibco, 31985-070). Separately, 5 µl of lipofectamine stem transfection reagent (Invitrogen, STEM00001) was mixed in 125 µl Opti-MEM. The diluted DNA and transfection reagent were then combined, mixed thoroughly, and allowed to incubate at room temperature for 30 min

before gently pipetting onto the cells. Cells were not passaged for at least 24 h after transfection.

Four days after transfection, cells were run on a Sony SH800 cell sorter (Sony Biotechnology). Single cells positive for the fluorescent selection marker were sorted into a flat-bottom, plastic 96-well plate (Corning, 353072) for the generation of clonal lines. These plates were left in the incubator for 7 days before screening colonies for fluorescent expression and morphology. Once propagated to a sufficient cell number, clonal lines were assayed for transgene functionality and for their ability to grow healthy gastruloids.

#### **Gastruloid protocol**

Gastruloids were grown in N2B27 media. This consists of a 1:1 mixture of DMEM/F-12 (Gibco, 11320033) and neurobasal medium (Gibco, 21103049), supplemented with 100  $\mu M$  2-mercaptoethanol, 1:100 N-2 (Gibco, 17502048), 1:50 B-27 (Gibco, 17504044) and 1:100 Pen Strep. Media was sterile-filtered using 0.22  $\mu m$  pore size Steriflip 50 ml conicals (Millipore Sigma, SCGP00525).

Gastruloid formation followed a standard protocol (Baillie-Johnson et al., 2015), one variation being that here we used a cell sorter to seed gastruloids as opposed to a hemocytometer and multichannel pipette. In short, a single-cell suspension of mESCs was washed twice in DPBS (–)Calcium (–)Magnesium to remove any trace amounts of 2i+ LIF media. This washed pellet was then resuspended in pre-warmed N2B27 media and run through a Sony SH800 cell sorter. The events were gated to exclude doublets and cell debris. Cells were sorted into a prepared 96-well, round-bottom, ultra-low attachment microplate (Corning, 7007). To minimize the effects of evaporation at the edges of the plate, the perimeter wells were filled with  $100~\mu l$  water containing 1:100~Pen~Strep. The inner 60 wells were then filled with  $40~\mu l$  N2B27. Two-hundred single mESCs were sorted into each of these 60 inner wells. The plate was then immediately returned to the incubator.

After 48 h, 150  $\mu$ l pre-warmed N2B27 with 3  $\mu$ M CHIR99021 was added to each gastruloid-containing well. At the 72-h mark, 150  $\mu$ l of media was removed from each well and replaced with 150  $\mu$ l fresh N2B27. Likewise, at the 96-h mark, 150  $\mu$ l of media was removed from each well and replaced with 150  $\mu$ l fresh N2B27. All inhibitor treatments were carried out between 96 and 120 h after aggregation. The inhibitors concentrations used in this study were as follows: 100 nM PD173074 (Selleck Chemicals, S1264), 1  $\mu$ M PD0325901 (Tocris, 4192), 10  $\mu$ M LY294002 (Cell Signaling Technology, 9901), 1  $\mu$ M MK-2206 (Selleck Chemicals, S1078), 10  $\mu$ M AG1296 (Selleck Chemicals, S8024) and 2  $\mu$ M OSI-906 (Selleck Chemicals, S1091). For global PI3K/Akt activation, platelet-derived growth factor-BB (Millipore Sigma, P3201) was used at 100 ng/ml. All doxycycline (Millipore Sigma, D9891) treatments were at a final concentration of 1  $\mu$ g/ml.

## Immunofluorescence staining

To stain adherent mESCs, media was aspirated and 4% paraformaldehyde in PBS (Fisher Scientific, AAJ19943K2) was added to fix the cells. After 15 min at room temperature, cells were washed with DPBS (–)Calcium (–)Magnesium, three times for 5 min per wash. DPBS was aspirated and PBSFT [10% fetal bovine serum and 0.2% Triton X-100 (Millipore Sigma, 648466) in DPBS] was added for 1 h at room temperature. After 1 h, PBSFT was aspirated and the primary antibody, diluted in PBSFT, was added to the cells. Cells were incubated in the primary antibody solution overnight at 4°C. The next day, the primary antibody solution was aspirated and the cells were washed three times in DPBS, 5 min per wash. The secondary antibody, diluted in PBSFT, was added to the cells and incubated for 90 min at room temperature. Cells were then washed another three times with PBS before imaging.

Staining of gastruloids followed a similar procedure (Baillie-Johnson et al., 2015). First, 150  $\mu$ l of media was removed from each well and replaced with 150  $\mu$ l of 4% PFA in PBS. Gastruloids were fixed at 4°C for 2 h, with continuous rocking. Then, 150  $\mu$ l was removed from each well and replaced with 150  $\mu$ l of DPBS (–)Calcium (–)Magnesium. This wash step was repeated for a total of three washes. Following the washes, gastruloids that were to undergo the same primary/secondary antibody staining regiment

were pooled into a single well of the round-bottom, 96-well plate. A 200 µl pipette with the tip cut off was used to transfer gastruloids under a dissection microscope. Once gastruloids were pooled (typically ten gastruloids per well), the PBS was completely removed from the well and replaced with PBSFT. Gastruloids were incubated in PBSFT overnight at 4°C. The following day, the PBSFT was removed from each well and replaced with the primary antibody diluted in PBSFT. Gastruloids were incubated in the primary antibody overnight at 4°C. The following day the primary antibody was washed out using PBSFT. This consisted of three short washes (~5 min intervals between washes) followed by three long washes (~1 h). After the final wash, the PBSFT was completely removed and replaced with the appropriate secondary antibody diluted in PBSFT. This was incubated overnight, and the following day the same wash procedure (three short, three long washes) was carried out. For any samples that were stained with DAPI (Thermo Fisher Scientific, 62248), 1 µg/ml DAPI was added with the secondary antibody.

Primary antibodies used in this work were: rabbit anti-phospho-p44/ 42 MAPK, Erk1/2 phosphorylated at Thr202 and Tyr204 (Cell Signaling Technology, 4370, 1:200), rabbit anti-phospho-Akt at Ser473 (Cell Signaling Technology, 9271, 1:400), rabbit anti-Snail C15D3 (Cell Signaling Technology, 3879, 1:50), rabbit anti-E-cadherin 24E10 (Cell Signaling Technology, 3195, 1:200), goat anti-brachyury (R&D Systems, AF2085, 10 µg/ml working concentration), rabbit anti-SOX2 (Cell Signaling Technology, 14962, 1:200), goat anti-TBX6 (R&D Systems, AF4744, 10 µg/ml working concentration), rabbit anti-GATA6 (Cell Signaling Technology, 5851, 1:500) and goat anti-SOX17 (R&D Systems, AF1924, 5 µg/ml working concentration). Secondary antibodies were: goat anti-rabbit Alexa Fluor 647 conjugate (Invitrogen, A27040, 1:500), chicken anti-goat Alexa Fluor 647 conjugate (Invitrogen, A21469, 1:500), goat anti-rabbit Alexa Fluor 405 conjugate (Invitrogen, A31556, 1:500) and donkey anti-rabbit Alexa Fluor 488 conjugate (Invitrogen A21206, 1:500).

#### **EdU** staining

EdU staining was performed using the 647 EdU Click Proliferation Kit (BD Biosciences, 565456). First, a 40 µM solution of EdU was made in prewarmed N2B27. Then, 95 µl of N2B27 was removed from each gastruloidcontaining well, and 95 µl of N2B27 containing EdU was added for a final concentration of 20 µM EdU in the well. The plate was returned to the incubator for 2 h to allow time for the EdU to integrate into S-phase cells. After 2 h, 150 µl of media was removed from each well and 150 µl of DPBS (-)Calcium (-)Magnesium was added to wash. Gastruloids were fixed by removing 150 µl from each well and replacing with 150 µl of 4% paraformaldehyde in PBS. Gastruloids were incubated in this solution for 1 h at 4°C, with continuous rocking. After fixation, gastruloids were washed three times with DPBS (-)Calcium (-)Magnesium. Then, as described previously, gastruloids of the same treatment conditions were pooled into one well of the 96-well plate (typically ten gastruloids/well). Once gastruloids were pooled, all liquid was removed, replaced with saponinbased permeabilization buffer and incubated overnight at 4°C. The following day, a working solution of the red 645 azide cocktail was prepared. For a final volume of 500 µl, 1 µl of azide dye was diluted into 24 μl DMSO. Into 435 μl DPBS (-)Calcium (-)Magnesium, 10 μl of copper catalyst solution, then 5 µl of diluted dye azide, then 50 µl of buffer additive were added. Then, all PBSFT was removed from the gastruloidcontaining wells and 100 µl of the azide cocktail was added to each well. The cocktail around the gastruloids was pipetted up and down in the well to ensure thorough mixing before incubation for 1 h at room temperature, with rotation and protected from light, mixing the solution again after 30 min. Once the incubation was complete, the azide cocktail was removed and gastruloids were washed three times with the saponin-based permeabilization buffer.

### Microscopy and staining quantification

All images in this work were acquired on a Nikon Eclipse Ti confocal microscope with a Prior linear motorized stage, a Yokogawa CSU-X1 spinning disk, an Agilent laser line module containing 405, 488, 561 and 650 nm lasers, and an iXon DU897 EMCCD camera.

For adherent cells, such as the dox-inducible myr-Akt and myr-SOScat lines, cells were plated on a 96-well, glass-bottom plate with high performance #1.5 cover glass (Cellvis, P96-1.5H-N) and were imaged using a 40× oil emersion objective. To image fixed gastruloids, first aggregates of the same experimental condition were pooled in plastic roundbottom wells. Then, all the gastruloids in a well were transferred to a single well of a glass-bottom plate (typically ten gastruloids per well). This pooling increased the efficiency of locating gastruloids on the microscope. Gastruloids were typically imaged using a 10× air objective. Stitched images were acquired if the gastruloids did not fit in a single frame. For stained gastruloids, 100 µm confocal image stacks were collected, with 10 µm steps, encompassing the volume from the bottom of the gastruloid where it contacted the glass to approximately the axial midline. Note that, when imaging fixed gastruloids, there was often aberrant material (fluorescent debris, well edges, or neighboring gastruloids) near the gastruloid being imaged. As such, for many sample images throughout the paper we cropped the background to remove these elements (see Fig. S7A). All image quantification, detailed below, was performed on raw images prior to background cropping. Imaging of stained gastruloids from a single experiment was carried out using identical imaging settings (e.g. laser powers, exposure times) and the same minimum-maximum scaling was used for every panel in the same figure comparing the same stain.

To quantify fluorescence profiles along the gastruloid major axis, first a maximum-intensity z-projection was obtained. Then, the gastruloid perimeter and major axis pixel coordinates were acquired in ImageJ, and these coordinates along with the maximum-intensity tif file were imported into MATLAB (MathWorks). Custom code was used to generate an arbitrary number (in this case, 200) of minor axis lines running perpendicular to the imported major axis, contained within the boundaries specified by the gastruloid perimeter. The average pixel intensity along each of these orthogonal lines was computed, thus providing a mean pixel intensity at discrete points along the major axis. These profiles were averaged for multiple gastruloids of the same experimental condition to generate average plots with standard deviations. To detect ppErk peaks in an unbiased manner, we used the MATLAB function 'findpeaks' to locate local maxima in the data. Gastruloid quantification code is available at https://github.com/toettchlab/Underhill2023. Note that, for all analyses, gastruloids were pooled and quantified without rejecting samples. Any difference between the number of gastruloids seeded and the number quantified per condition is a result of losses during the fixation and staining process. Starting numbers of gastruloids for each experiment are indicated in the figure captions. In the minor fraction of gastruloids with multiple posterior poles, the dominant pole was selected for quantification. For a full tabulation of gastruloid numbers and replicates per experiment, see Table S1.

### **Live imaging**

All time-lapse experiments were performed with gastruloids embedded in 50% Matrigel (Corning, 356231)/50% N2B27 by volume to restrict lateral movement of the gastruloid during imaging. The following protocol was adapted from that of van den Brink et al. (2020). To prepare for live imaging, Matrigel was first thawed at 4°C overnight. Note that Matrigel must be kept cold to prevent polymerization and solidification. The following day 50% Matrigel/50% N2B27 solution was prepared in a 4°C room. This mixture was pipetted into the center coverslip region of a 35 mm glass-bottom imaging dish (Ibidi, 81218). A flat metal object was placed on top of a bucket full of the ice and the imaging dish placed on top of the metal. This facilitates heat transfer, keeping the Matrigel cold. At a dissection microscope, individual gastruloids were pipetted up using a 200 µl pipette with the tip cut off. The desired amount of gastruloids were deposited into the Matrigel in the center of the imaging dish. If the gastruloids were clumped together they were gently pipetted up from the Matrigel and distributed more evenly. Once this was complete, the dish was placed in an incubator at 37°C for 10 min, allowing the Matrigel to solidify. Then, 2 ml of pre-warmed N2B27 was added to the dish.

Gastruloids were maintained at 37°C with 5% CO<sub>2</sub> for the duration of all time-lapse experiments using an environmental control unit (Okolab). The media in the imaging dish was covered with mineral oil (Sigma-Aldrich,

330779) to prevent evaporation. The microscope was configured for DIC microscopy for live imaging. Images were acquired using a  $20\times$  air objective.

PIV outputs were generated using the MATLAB application PIVlab (Thielicke and Sonntag, 2021). Analysis was performed on 1 h of data preceding the time stamp on the figure. Masks were drawn on the image to exclude background, and a fast-Fourier transform-based multipass algorithm was used to generate the velocity field for a given pair of frames. The mean velocity vector is displayed on the plot, and the heat map represents velocity magnitude at a given position.

#### **Gastruloid cell counting**

A Countess II automated cell counter (Thermo Fisher Scientific) was used for all cell-counting experiments. First, gastruloids were pooled into a single well of a round-bottom, plastic 96-well plate. Pooling gastruloids provided a sufficient number of cells to obtain an accurate cell count. Between five and ten gastruloids were pooled per measurement, depending on the experiment (see figure captions for experiment-specific values). All of the media was removed from the wells, and gastruloids were washed with 200 µl DPBS (-)Calcium (-)Magnesium, then transferred in the solution to a microcentrifuge tube. This was centrifuged at 400 g for 5 min to pellet the gastruloids. The supernatant was then aspirated, and 100 µl TrypLE Express Enzyme was added to each tube, pipetting with sufficient force to disturb the gastruloid pellet. The samples were incubated in a 37°C bead bath for 5 min, then the solution was pipetted up and down to break gastruloids into a single-cell suspension. Next, 100 µl of 0.4% Trypan Blue solution (Gibco, 15250061) was added to each sample, and the samples were run on the automated cell counter to quantify total cell number and the percentage of live/dead cells. We validated the cell counts obtained by automated cell counting using a hemocytometer, obtaining values within 10% using both techniques.

#### Acknowledgements

We thank members of the Toettcher laboratory, particularly Harry McNamara, for insightful comments and suggestions. We also thank Alfonso Martinez Arias for generously sharing mESC lines and gastruloid protocols.

#### Competing interests

J.E.T. is a scientific advisor for Prolific Machines and Nereid Therapeutics. The remaining authors declare no conflicts of interest.

### **Author contributions**

Conceptualization: E.J.U., J.E.T.; Methodology: E.J.U.; Software: E.J.U.; Investigation: E.J.U.; Writing - original draft: E.J.U., J.E.T.; Writing - review & editing: J.E.T.; Visualization: E.J.U.; Supervision: J.E.T.; Project administration: J.E.T.; Funding acquisition: J.E.T.

#### Funding

This work was supported by a National Science Foundation CAREER Award (1750663 to J.E.T.) and a National Science Foundation RECODE grant (2134935).

#### Data availability

All relevant data can be found within the article and its supplementary information.

#### Peer review history

The peer review history is available online at https://journals.biologists.com/dev/lookup/doi/10.1242/dev.201663.reviewer-comments.pdf.

#### References

- Anand, G. M., Megale, H. C., Murphy, S. H., Weis, T., Lin, Z., He, Y., Wang, X., Liu, J. and Ramanathan, S. (2023). Controlling organoid symmetry breaking uncovers an excitable system underlying human axial elongation. *Cell* 186, 497-512.e23. doi:10.1016/j.cell.2022.12.043
- Baillie-Johnson, P., Van Den Brink, S. C., Balayo, T., Turner, D. A. and Martinez Arias, A. (2015). Generation of aggregates of mouse embryonic stem cells that show symmetry breaking, polarization and emergent collective behaviour in vitro. J. Vis. Exp. 105, 53252. doi:10.3791/53252
- Barriga, E. H. and Mayor, R. (2019). Adjustable viscoelasticity allows for efficient collective cell migration. Semin. Cell Dev. Biol. 93, 55-68. doi:10.1016/j.semcdb. 2018.05.027

- Beccari, L., Moris, N., Girgin, M., Turner, D. A., Baillie-Johnson, P., Cossy, A.-C., Lutolf, M. P., Duboule, D. and Arias, A. M. (2018). Multi-axial self-organization properties of mouse embryonic stem cells into gastruloids. *Nature* 562, 272-276. doi:10.1038/s41586-018-0578-0
- **Boulet, A. M. and Capecchi, M. R.** (2012). Signaling by FGF4 and FGF8 is required for axial elongation of the mouse embryo. *Dev. Biol.* **371**, 235-245. doi:10.1016/j. ydbio.2012.08.017
- Brewer, J. R., Mazot, P. and Soriano, P. (2016). Genetic insights into the mechanisms of Fgf signaling. *Genes Dev.* 30, 751-771. doi:10.1101/gad.277137.
- Chapman, D. L., Agulnik, I., Hancock, S., Silver, L. M. and Papaioannou, V. E. (1996). Tbx6, a mouse T-box gene implicated in paraxial mesoderm formation at gastrulation. *Dev. Biol.* 180, 534-542. doi:10.1006/dbio.1996.0326
- Chazaud, C., Yamanaka, Y., Pawson, T. and Rossant, J. (2006). Early lineage segregation between epiblast and primitive endoderm in mouse blastocysts through the Grb2-MAPK pathway. Dev. Cell 10, 615-624. doi:10.1016/j.devcel.2006.02.020
- Ciruna, B. and Rossant, J. (2001). FGF signaling regulates mesoderm cell fate specification and morphogenetic movement at the primitive streak. *Dev. Cell* 1, 37-49. doi:10.1016/S1534-5807(01)00017-X
- Ciruna, B. G., Schwartz, L., Harpal, K., Yamaguchi, T. P. and Rossant, J. (1997). Chimeric analysis of fibroblast growth factor receptor-1 (Fgfr1) function: a role for FGFR1 in morphogenetic movement through the primitive streak. *Development* **124**, 2829-2841. doi:10.1242/dev.124.14.2829
- Cunningham, T. J., Brade, T., Sandell, L. L., Lewandoski, M., Trainor, P. A., Colas, A., Mercola, M. and Duester, G. (2015). Retinoic acid activity in undifferentiated neural progenitors is sufficient to fulfill its role in restricting Fgf8 expression for somitogenesis. PLoS ONE 10, e0137894. doi:10.1371/journal.pone.0137894
- Dubrulle, J. and Pourquié, O. (2004). fgf8 mRNA decay establishes a gradient that couples axial elongation to patterning in the vertebrate embryo. *Nature* 427, 419-422. doi:10.1038/nature02216
- Ellis, P., Fagan, B. M., Magness, S. T., Hutton, S., Taranova, O., Hayashi, S., Mcmahon, A., Rao, M. and Pevny, L. (2004). SOX2, a persistent marker for multipotential neural stem cells derived from embryonic stem cells, the embryo or the adult. *Dev. Neurosci.* 26, 148-165. doi:10.1159/000082134
- Engert, S., Liao, W. P., Burtscher, I. and Lickert, H. (2009). Sox17-2A-iCre: A knock-in mouse line expressing Cre recombinase in endoderm and vascular endothelial cells. *Genesis* 47, 603-610. doi:10.1002/dvg.20540
- Fehling, H. J., Lacaud, G., Kubo, A., Kennedy, M., Robertson, S., Keller, G. and Kouskoff, V. (2003). Tracking mesoderm induction and its specification to the hemangioblast during embryonic stem cell differentiation. *Development* 130, 4217-4227. doi:10.1242/dev.00589
- Garriock, R. J., Chalamalasetty, R. B., Kennedy, M. W., Canizales, L. C., Lewandoski, M. and Yamaguchi, T. P. (2015). Lineage tracing of neuromesodermal progenitors reveals novel Wnt-dependent roles in trunk progenitor cell maintenance and differentiation. *Development* 142, 1628-1638. doi:10.1242/dev.111922
- Grusch, M., Schelch, K., Riedler, R., Reichhart, E., Differ, C., Berger, W., Inglés-Prieto, Á. and Janovjak, H. (2014). Spatio-temporally precise activation of engineered receptor tyrosine kinases by light. *EMBO J.* 33, 1713-1726. doi:10. 15252/embj.201387695
- Gureasko, J., Galush, W. J., Boykevisch, S., Sondermann, H., Bar-Sagi, D., Groves, J. T. and Kuriyan, J. (2008). Membrane-dependent signal integration by the Ras activator Son of sevenless. *Nat. Struct. Mol. Biol.* 15, 452-461. doi:10. 1038/nsmb.1418
- Hashmi, A., Tlili, S., Perrin, P., Lowndes, M., Peradziryi, H., Brickman, J. M., Martínez Arias, A. and Lenne, P.-F. (2022). Cell-state transitions and collective cell movement generate an endoderm-like region in gastruloids. *eLife* 11, e59371. doi:10.7554/eLife.59371
- Kanai-Azuma, M., Kanai, Y., Gad, J. M., Tajima, Y., Taya, C., Kurohmaru, M., Sanai, Y., Yonekawa, H., Yazaki, K., Tam, P. P. L. et al. (2002). Depletion of definitive gut endoderm in Sox17-null mutant mice. *Development* 129, 2367-2379. doi:10.1242/dev.129.10.2367
- Kattman, S. J., Huber, T. L. and Keller, G. M. (2006). Multipotent Flk-1<sup>+</sup> cardiovascular progenitor cells give rise to the cardiomyocyte, endothelial, and vascular smooth muscle lineages. *Dev. Cell* 11, 723-732. doi:10.1016/j.devcel. 2006.10.002
- Kim, N., Kim, J. M., Lee, M., Kim, C. Y., Chang, K.-Y. and Heo, W. D. (2014). Spatiotemporal control of fibroblast growth factor receptor signals by blue light. Chem. Biol. 21, 903-912. doi:10.1016/j.chembiol.2014.05.013
- Li, W. X. (2005). Functions and mechanisms of receptor tyrosine kinase Torso signaling: lessons from Drosophila embryonic terminal development. *Dev. Dyn.* 232, 656-672. doi:10.1002/dydy.20295
- Matsui, T., Kanai-Azuma, M., Hara, K., Matoba, S., Hiramatsu, R., Kawakami, H., Kurohmaru, M., Koopman, P. and Kanai, Y. (2006). Redundant roles of Sox17 and Sox18 in postnatal angiogenesis in mice. *J. Cell Sci.* 119, 3513-3526. doi:10.1242/ics.03081
- Mendoza, M. C., Er, E. E. and Blenis, J. (2011). The Ras-ERK and PI3K-mTOR pathways: cross-talk and compensation. *Trends Biochem. Sci.* **36**, 320-328. doi:10.1016/j.tibs.2011.03.006

- Merle, M., Friedman, L., Chureau, C. and Gregor, T. (2023). Precise and scalable self-organization in mammalian pseudo-embryos. arXiv doi:10.48550/arXiv.2303. 17522
- Molotkov, A. and Soriano, P. (2018). Distinct mechanisms for PDGF and FGF signaling in primitive endoderm development. *Dev. Biol.* 442, 155-161. doi:10. 1016/j.vdbio.2018.07.010
- Morrisey, E. E., Ip, H. S., Lu, M. M. and Parmacek, M. S. (1996). GATA-6: a zinc finger transcription factor that is expressed in multiple cell lineages derived from lateral mesoderm. *Dev. Biol.* 177, 309-322. doi:10.1006/dbio.1996.0165
- Ng, Y., Ramm, G., Lopez, J. A. and James, D. E. (2008). Rapid activation of Akt2 is sufficient to stimulate GLUT4 translocation in 3T3-L1 adipocytes. *Cell Metab.* 7, 348-356. doi:10.1016/j.cmet.2008.02.008
- Niwa, Y., Shimojo, H., Isomura, A., González, A., Miyachi, H. and Kageyama, R. (2011). Different types of oscillations in Notch and Fgf signaling regulate the spatiotemporal periodicity of somitogenesis. *Genes Dev.* 25, 1115-1120. doi:10.1101/gad.2035311
- Regot, S., Hughey, J. J., Bajar, B. T., Carrasco, S. and Covert, M. W. (2014). High-sensitivity measurements of multiple kinase activities in live single cells. *Cell* **157**, 1724-1734. doi:10.1016/j.cell.2014.04.039
- Riley, J. K., Carayannopoulos, M. O., Wyman, A. H., Chi, M. and Moley, K. H. (2006). Phosphatidylinositol 3-kinase activity is critical for glucose metabolism and embryo survival in murine blastocysts. *J. Biol. Chem.* **281**, 6010-6019. doi:10. 1074/jbc.M506982200
- Rossi, G., Broguiere, N., Miyamoto, M., Boni, A., Guiet, R., Girgin, M., Kelly, R. G., Kwon, C. and Lutolf, M. P. (2021). Capturing cardiogenesis in gastruloids. *Cell Stem Cell* **28**, 230-240.e6. doi:10.1016/j.stem.2020.10.013
- Sun, X., Meyers, E. N., Lewandoski, M. and Martin, G. R. (1999). Targeted disruption of Fgf8 causes failure of cell migration in the gastrulating mouse embryo. *Genes Dev.* 13, 1834-1846. doi:10.1101/gad.13.14.1834
- Suppinger, S., Zinner, M., Aizarani, N., Lukonin, I., Ortiz, R., Azzi, C., Stadler, M. B., Vianello, S., Palla, G., Kohler, H. et al. (2023). Multimodal characterization of murine gastruloid development. *Cell Stem Cell* 30, 867-884.e11. doi:10.1016/j. stem.2023.04.018
- Thielicke, W. and Sonntag, R. (2021). Particle Image Velocimetry for MATLAB: accuracy and enhanced algorithms in PIVIab. J. Open Res. Softw. 9, 12. doi:10. 5334/iors.334
- Toettcher, J. E., Weiner, O. D. and Lim, W. A. (2013). Using optogenetics to interrogate the dynamic control of signal transmission by the Ras/Erk module. *Cell* 155, 1422-1434. doi:10.1016/j.cell.2013.11.004
- Turner, D. A., Glodowski, C. R., Alonso-Crisostomo, L., Baillie-Johnson, P., Hayward, P. C., Collignon, J., Gustavsen, C., Serup, P., Schröter, C. and Arias, A. M. (2016). Interactions between Nodal and Wnt signalling drive robust symmetry-breaking and axial organisation in gastruloids (embryonic organoids). bioRxiv doi:10.1101/051722

- Tzouanacou, E., Wegener, A., Wymeersch, F. J., Wilson, V. and Nicolas, J.-F. (2009). Redefining the progression of lineage segregations during mammalian embryogenesis by clonal analysis. *Dev. Cell* 17, 365-376. doi:10.1016/j.devcel. 2009.08.002
- Van Den Brink, S. C., Baillie-Johnson, P., Balayo, T., Hadjantonakis, A.-K., Nowotschin, S., Turner, D. A. and Martinez Arias, A. (2014). Symmetry breaking, germ layer specification and axial organisation in aggregates of mouse embryonic stem cells. *Development* 141, 4231-4242. doi:10.1242/dev.113001
- Van Den Brink, S. C., Alemany, A., Van Batenburg, V., Moris, N., Blotenburg, M., Vivié, J., Baillie-Johnson, P., Nichols, J., Sonnen, K. F., Martinez Arias, A. et al. (2020). Single-cell and spatial transcriptomics reveal somitogenesis in gastruloids. *Nature* 582, 405-409. doi:10.1038/s41586-020-2024-3
- Van Stry, M., Kazlauskas, A., Schreiber, S. L. and Symes, K. (2005). Distinct effectors of platelet-derived growth factor receptor-α signaling are required for cell survival during embryogenesis. *Proc. Natl. Acad. Sci. USA* 102, 8233-8238. doi:10.1073/pnas.0502885102
- Veenvliet, J. V., Bolondi, A., Kretzmer, H., Haut, L., Scholze-Wittler, M., Schifferl, D., Koch, F., Guignard, L., Kumar, A. S., Pustet, M. et al. (2020). Mouse embryonic stem cells self-organize into trunk-like structures with neural tube and somites. Science 370, eaba4937. doi:10.1126/science.aba4937
- Vianello, S. and Lutolf, M. P. (2020). In vitro endoderm emergence and selforganisation in the absence of extraembryonic tissues and embryonic architecture. bioRxiv. doi:10.1101/2020.06.07.138883
- Wang, Q., Fan, H., Li, F., Skeeters, S. S., Krishnamurthy, V. V., Song, Y. and Zhang, K. (2020). Optical control of ERK and AKT signaling promotes axon regeneration and functional recovery of PNS and CNS in Drosophila. *eLife* 9, e57395. doi:10.7554/eLife.57395.sa2
- Wood, H. B. and Episkopou, V. (1999). Comparative expression of the mouse Sox1, Sox2 and Sox3 genes from pre-gastrulation to early somite stages. *Mech. Dev.* 86, 197-201. doi:10.1016/S0925-4773(99)00116-1
- Yamaguchi, T. P., Harpal, K., Henkemeyer, M. and Rossant, J. (1994). fgfr-1 is required for embryonic growth and mesodermal patterning during mouse gastrulation. *Genes Dev.* 8, 3032-3044. doi:10.1101/gad.8.24.3032
- Yaman, Y. I. and Ramanathan, S. (2023). Controlling human organoid symmetry breaking reveals signaling gradients drive segmentation clock waves. *Cell* 186, 513-527.e19. doi:10.1016/j.cell.2022.12.042
- Yamanaka, Y., Hamidi, S., Yoshioka-Kobayashi, K., Munira, S., Sunadome, K., Zhang, Y., Kurokawa, Y., Ericsson, R., Mieda, A., Thompson, J. L. et al. (2023). Reconstituting human somitogenesis in vitro. *Nature*. **614**, 509-520. doi:10.1038/s41586-022-05649-2
- Yang, X., Chrisman, H. and Weijer, C. J. (2008). PDGF signalling controls the migration of mesoderm cells during chick gastrulation by regulating N-cadherin expression. *Development* 135, 3521-3530. doi:10.1242/dev.023416